Soft Matter

Focal conic flowers, dislocation rings, and undulation textures in smectic liquid crystal Janus droplets

Journal:	*Soft Matter*
Manuscript ID	SM-ART-11-2021-001623.R2
Article Type:	Paper
Date Submitted by the Author:	12-May-2022
Complete List of Authors:	Wei, Wei-Shao; University of Pennsylvania, Department of Physics and Astronomy; University of Pennsylvania, Laboratory for Research on the Structure of Matter Jeong, Joonwoo; Ulsan National Institute of Science and Techonology, Physics Collings, Peter; Swarthmore College, Physics & Astronomy Yodh, Arjun; University of Pennsylvania, Department of Physics

Soft Matter

ARTICLE TYPE

Cite this: DOI: 00.0000/xxxxxxxxxx

Focal conic flowers, dislocation rings, and undulation textures in smectic liquid crystal Janus droplets†

Wei-Shao Wei,*[a,b]‡ Joonwoo Jeong,*[c] Peter J. Collings,[a,d] and A. G. Yodh[a,b]

Received Date
Accepted Date

DOI: 00.0000/xxxxxxxxxx

Liquid crystalline phases of matter often exhibit visually stunning patterns or textures. Mostly, these liquid crystal (LC) configurations are uniquely determined by bulk LC elasticity, surface anchoring conditions, and confinement geometry. Here, we experimentally explore defect textures of the smectic LC phase in unique confining geometries with variable curvature. We show that a complex range of director configurations can arise from a single system, depending on sample processing procedures. Specifically, we report on LC textures in Janus drops comprised of silicone oil and 8CB in its smectic-A LC phase. The Janus droplets were made in aqueous suspension using solvent-induced phase separation. After drop creation, smectic layers form in the LC compartment, but their self-assembly is frustrated by the need to accommodate both the bowl-shaped cavity geometry and homeotropic (perpendicular) anchoring conditions at boundaries. A variety of stable and *metastable* smectic textures arise, including focal conic domains, dislocation rings, and undulations. We experimentally characterize their stabilities and follow their spatiotemporal *evolution*. Overall, a range of fabrication kinetics produce very different intermediate and final states. The observations elucidate assembly mechanisms and suggest new routes for fabrication of complex soft material structures in Janus drops and other confinement geometries.

1 Introduction

Liquid crystals (LCs) are technologically important soft phases of matter wherein constituent rod- or disk-like molecules retain long-range orientational order and sometimes partial positional order. For decades, these anisotropic soft materials have yielded surprises, including delicate textures, complex phase behavior, and unusual packings within drops.[1–8] Some current interest centers on experiments that confine LCs in tiny "containers" with controllable geometry and boundary conditions. These scenarios offer novel playgrounds to probe fundamental questions about LC assembly and response to frustration.[9–11] In this context, smectic LC phases are particularly interesting and much less studied than nematic phases.

Briefly, smectic LC phases form layered structures and are thus endowed with potential to exhibit translational and orientational order. By comparison, the simpler nematic LC phase possesses only orientational order characterized by its director field $\hat{\mathbf{n}}$. In the smectic-A (SmA) phase, for example, constituent molecules tend to arrange in layers with their long molecular axis parallel to the layer normal (see inset of Fig. 1(a)). In large, open, and "ideal" bulk samples, these layers typically stack in parallel planes, making a one-dimensional (1D) quasi-solid (*i.e.*, a soft solid). Another layer-stacking configuration, found in spheres with perpendicular surface anchoring, is called an onion texture.[12,13] In still other confined geometries with various boundary conditions, SmA LCs can self-assemble into more complicated textures; one such texture that relieves frustration in a mathematically elegant way is called the focal conic domain (FCD).[14–28]

In this contribution, we explore the textures of 4'-octyl-4-biphenylcarbonitrile (8CB) in the SmA phase, within bowl-shaped cavities of Janus droplets with *homeotropic* boundary conditions wherein molecular orientation is perpendicular to the interface. Previously, we have reported on fabrication methods and observations associated with nematic LC Janus droplets (of 4'-pentyl-4-biphenylcarbonitrile, 5CB).[29] Here we use similar synthesis procedures to create Janus drops with SmA LCs. The resulting LC textures in these compartments are very different from those of the nematic phase. Our study shares similarities with experiments recently reported by Concellón *et al.*,[28] which included a study of SmA Janus drops with controlled anchoring conditions. They reported formation of FCD defects via anchoring-dominated mechanisms. Here we focus on the role of curvature in producing di-

[a] *Department of Physics and Astronomy, University of Pennsylvania, Philadelphia, PA, USA. E-mail: weiwe@sas.upenn.edu*
[b] *Laboratory for Research on the Structure of Matter (LRSM), University of Pennsylvania, Philadelphia, PA, USA.*
[c] *Department of Physics, Ulsan National Institute of Science and Technology (UNIST), Ulsan, Republic of Korea. E-mail: jjeong@unist.ac.kr*
[d] *Department of Physics and Astronomy, Swarthmore College, Swarthmore, PA, USA.*
† Electronic Supplementary Information (ESI) available: Supplementary Figure S1-5 and Supplementary Video 1-4. See DOI: 10.1039/cXsm00000x/
‡ Present address: E-mail: wswei@brandeis.edu

rector configurations and topological defects in the smectic LCs with pure homeotropic anchoring. The resulting defect textures depend strongly on confining *geometry* and fabrication kinetics, and rather weakly on interfacial anchoring. Notably, this system holds potential to support and manipulate a variety of unexplored LC textures in suspended droplets.

The experiments reveal formation of three classes of director and layer configurations in the smectic LC compartment of the Janus drops. After initial creation of the Janus drop, flower textures associated with FCDs, ring textures associated with dislocation defects, and textures with both undulations and dislocation rings, all arise. These textures result from novel geometries of the Janus droplet, wherein varying curvature of the compartment disrupts the parallel stacking of the SmA layers. To our knowledge, textures with FCD packings have never been observed in suspended emulsion droplets *without* planar anchoring; evidently, compartment curvature drives FCD formation in systems with homeotropic anchoring. The textures remain stable without further disturbance. However, annealing of the drops enables us to drive the system towards lower free energy states. Our observations suggest that the texture with dislocation rings plus smectic layer undulations is the lower energy state, and that the FCD and dislocation ring textures could be metastable. We experimentally map out the drop conditions for which particular textures are more (or less) likely to form, and we rationalize these observations. The study provides insight about frustration relief and suggests routes for guiding smectic LCs into potentially useful new forms, which could have value for functional LC materials. The new information gleaned also teaches us about how to use assembly kinetics for fabrication of specific soft matter intermediate states.

2 Materials and Methods

2.1 Preparation of the SmA LC Janus droplets

The scheme we employ to fabricate droplets with immiscible LC and non-LC compartments shares features with our prior work.[29] Generally, the final morphology of the drop is sensitive to several factors including compartment volume ratio, the interfacial tensions of the immiscible fluids, surfactant type, and surfactant concentration in the background aqueous phase. Here we deploy 8CB as the LC compartment (with its well-known temperature-dependent phase behavior), and we use silicone oil (polydimethylsiloxane, PDMS) for the isotropic compartment.

The LC Janus droplets were made in three steps. First (step 1), we prepared (spherical) emulsion droplets containing fully miscible homogeneous mixtures of 8CB, PDMS, and hexane, and we suspended these precursor organic liquid drops in an aqueous solution. Second (step 2), we made Janus droplets from the emulsion-drop precursors via solvent-induced phase separation within individual droplets. Finally, in the last step (step 3), we thermally annealed the samples to permit the Janus droplets to evolve to their lowest free energy state. These three steps are described in more detail below.

Step 1:

A 1:1 by weight mixture of 4'-octyl-4-biphenylcarbonitrile (8CB, Kingston Chemicals Ltd.) and polydimethylsiloxane (silicone oil PDMS, viscosity 10,000 cSt at 25 °C, Sigma-Aldrich) was dissolved in hexane (organic solvent, Fisher Scientific) to make a homogeneous organic phase mixture. The total concentration of 8CB and PDMS within hexane is 5% (wt/vol). Because the density of 8CB and PDMS is similar, the mass ratio is approximated accurately as the volume ratio. A surfactant, sodium dodecyl sulfate (SDS, Sigma-Aldrich), was dissolved in deionized water to make the background continuous aqueous phase with a surfactant concentration of 0.1% by weight (below the SDS critical micelle concentration, CMC). All chemicals were used as received, without further purification/modification.

The fully miscible homogeneous organic liquid mixture was then converted into a micro-emulsion droplet suspension in the background aqueous solution via two different methods. The first method entailed simply shaking the organic liquid mixture in the aqueous solution to create a polydisperse distribution of droplets. The second method used capillary microfluidics[30] to create monodisperse droplets. The volume fraction of the

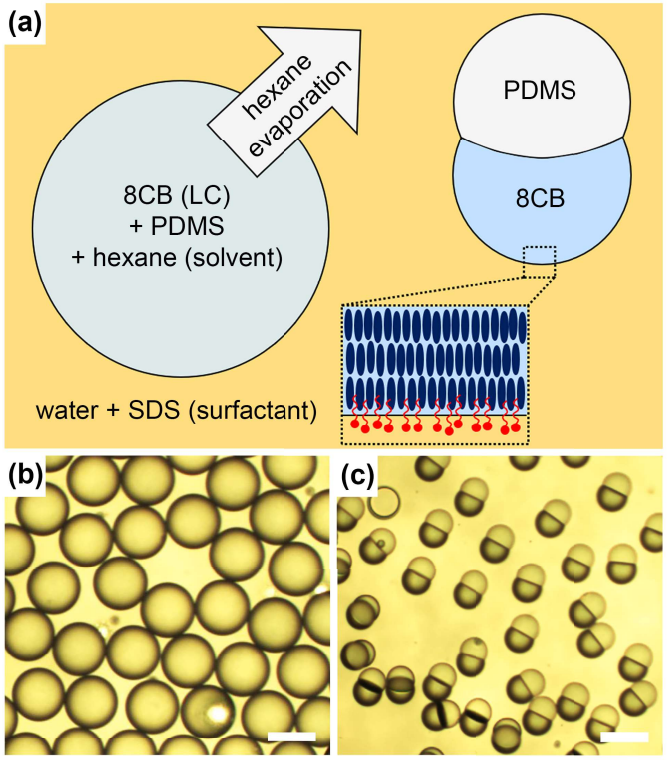

Fig. 1 Preparation of SmA LC Janus droplets via solvent-induced phase separation. (a) Schematic shows how solvent-induced phase separation leads to formation of Janus droplets with two immiscible compartments: 8CB and PDMS. The initial droplet (left) after emulsification contains a homogeneous organic liquid mixture of 8CB, PDMS, and hexane. The droplet is stabilized by a surfactant SDS and suspended in the aqueous solution. Evaporation of the organic solvent, hexane, though the background phase gives the target Janus droplet (right). Inset: A closer look at the surfactant-stabilized 8CB-water interface. The red symbols represent surfactant molecules. Dark blue ellipses represent 8CB molecules; the SmA layers are illustrated. (b-c) Bright-field microscopy images of (b) the initial homogeneous droplets and (c) the final Janus droplets after phase separation. In (c), the darker droplet compartments contain 8CB. Scale bar: 50 μm.

8CB/PDMS/hexane organic liquid mixture in the SDS aqueous solution was approximately 10%. At this stage, the suspended droplets have spherical shape and contain a homogeneous miscible mixture of 8CB, PDMS, and hexane (see the left panel of Fig. 1(a) and Fig. 1(b)).

Step 2:

The 8CB/PDMS/hexane droplets suspended in SDS aqueous solution were introduced into uncovered glass wells. The sample wells were then stored overnight, *i.e.*, ∼12 hours, in a custom-built chamber at 100% relative humidity. This setup expedites evaporation of hexane from the droplets and minimizes evaporation of water from the surfactant solution. Note, throughout the process of hexane evaporation, we believe the evaporation of water from the solutions containing SDS surfactant was negligible.

The complete evaporation of hexane causes separation of the immiscible 8CB and PDMS fluids within the drops. Then formation of the Janus droplets readily occurs (see the right panel of Fig. 1(a) and Fig. 1(c)). The Janus droplets made by shaking had diameters ranging from 10 to 70 μm; the monodisperse droplets made via capillary microfluidics typically had a radius of 15.4 μm that depended on dimensions of the microfluidics set-up and the fluid flow rates. We then transferred the Janus droplet suspensions to rectangular capillaries (0.4 mm height and 4 mm width, VitroCom), sealed them with glue, and stored them at room temperature for 24 hours before observation.

Note, at this stage, "quenched" Janus droplets are generated with smectic 8CB confined in the bowl-shaped cavities. (Further discussion about the precise meaning of quench is given later in the *Results and Discussion* section.) Analysis of the resultant LC configurations/textures and droplet morphologies was then carried out.

Step 3:

The samples obtained in Step 2 were first studied optically. Subsequently, they were annealed (quickly heated to 45 °C and then slowly cooled to room temperature again). This annealing procedure enhances the probability for generating equilibrium LC textures. We call these latter stage drops as "annealed" Janus droplets. The resultant annealed LC textures and droplet morphologies were again studied using optical microscopy.

Lastly, some of the annealed Janus droplets were stored and allowed to relax at room temperature for a few more days, and then they were inspected by optical microscopy again.

2.2 Analysis of SmA LC configurations and textures within Janus droplets

Sample cells containing SmA LC Janus droplets were observed with a Leica DMIR13 inverted optical microscope in bright-field and polarization optical microscopy (POM) modes. Leica N Plan 10×, Leica PL Fluotar L 63×, and Leica PL APO 100× objectives were used. Crossed-polarizers and full-wave retardation plates were deployed in the microscope to characterize LC director configurations within the droplets (Fig. 2(a)).

Note, because of the slight density difference between the two compartments, the Janus droplets rotate and align with the denser material, 8CB, closer to the surface of the earth. Thus, optical images taken by the inverted optical microscope are mostly bottom-view images of droplets, wherein the LC filled bowl-shaped (spherical-cap-like) cavity resides symmetrically in the part of the drop closest to the surface of the earth. Note, LC birefringence and the curved interfaces of the droplet typically cause some image distortion.

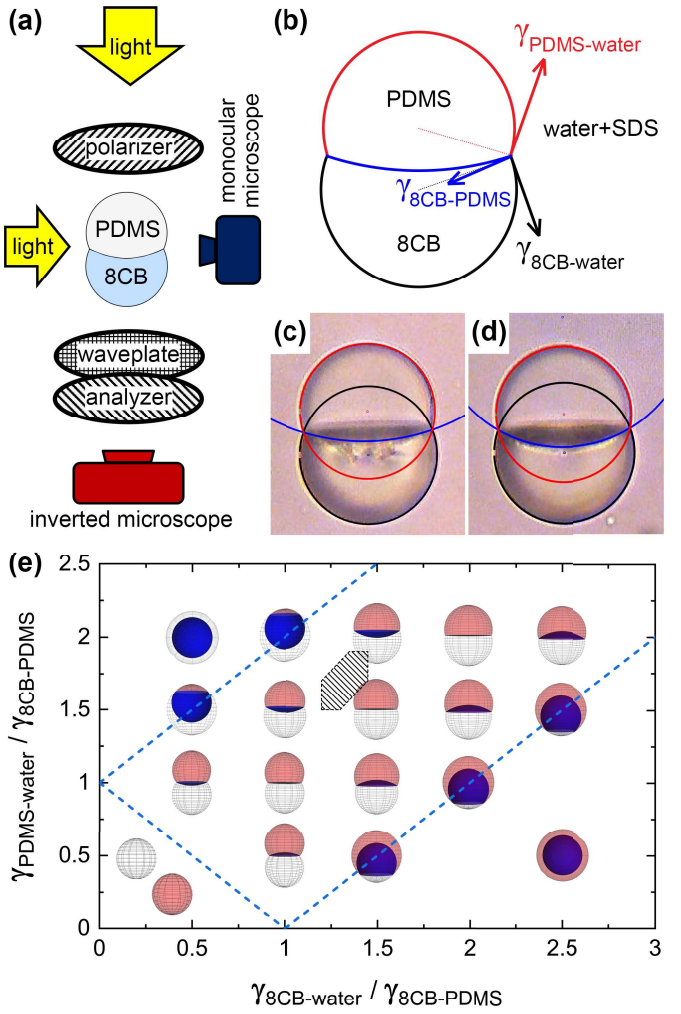

Fig. 2 Morphology profiles of the SmA LC Janus droplets. (a) Schematic of the experimental setup. Bottom-view and side-view images of individual Janus droplet were taken by an inverted optical microscope (dark red, with crossed polarizers and full-wave retardation plate) and a turned monocular microscope (dark blue), respectively. (b) Schematic of a side-viewed Janus droplet. At the three-phase boundary, $\gamma_{8CB-PDMS}$, $\gamma_{8CB-water}$, and $\gamma_{PDMS-water}$ denotes interfacial tension for the 8CB-PDMS, 8CB-water (SDS aqueous solution), and PDMS-water (SDS aqueous solution) interfaces, respectively. For easier recognition, individual interfacial tension and its corresponding interface are labeled with blue, black, and red color, respectively. (c-d) Exemplary side-view images of SmA Janus droplets containing (c) FCD flower textures and (d) dislocation ring textures. Representative circle-fits used to extract the interfacial tension ratios are also illustrated, with the same color code as (b). Drop radius: 15.4 μm. (e) The droplet morphology state diagram with respect to interfacial tension ratios. The volume ratio between 8CB and PDMS is fixed to be unity. Blue dashed lines represent the boundaries in a Janus droplet, in a core-shell (top left and bottom right) droplet, and in two detached droplets (bottom left). The region denoted by black diagonal hatch pattern roughly encloses our experimental regime. Inset: color coded 3D drop reconstructions.

2.3 Analysis of Janus droplet morphologies

Side-view images of SmA LC Janus droplets, aligned by gravity, were also recorded using a small and portable Bausch and Lomb monocular microscope operating in bright-field mode; this microscope was equipped with a 43× air objective. We obtained these measurements by turning the monocular microscope (together with the mounted sample cell) on its side and then taking side-view images of the Janus droplets (Fig. 2(a)). We determined and analyzed the droplet morphologies by fitting the drop profiles as detailed below.

Generally, the morphologies of the compartments within the Janus droplets are determined by the relative values of the interfacial tension between the two immiscible compartment liquids (*i.e.*, 8CB and PDMS) and the third immiscible background liquid (*i.e.*, the SDS-water solution). In equilibrium, the three-phase boundary adopts a unique configuration, requiring a vector sum of the three interfacial tensions to be zero; this condition is known as Neumann's triangle (see Fig. 2(b)). Experimentally, the ratios between three interfacial tensions $\gamma_{8\mathrm{CB-PDMS}}$, $\gamma_{8\mathrm{CB-water}}$, and $\gamma_{\mathrm{PDMS-water}}$ are characterized by the contact angles at the junction point. We determined the contact angles by fitting each phase boundary to an arc[31] (see examples in Fig. 2(c) and Fig. 2(d)). Specifically, the arc is the best fit for a set of three points on each interface, including the two intersection points on the three-phase boundary. We excluded data when either of the two intersection points is not readily apparent, or when there is recognizable disagreement between the best fit and corresponding interface, or when the calculated volume ratio between compartments substantially disagrees with experimental parameters. The latter two situations could arise from Janus droplets whose symmetry axes are not fully aligned with gravity, or from image distortions arising near the 8CB-PDMS boundary (*e.g.*, due to LC birefringence).

Note, the equilibrium droplet shape depends on energetics associated with both interfacial tension and bulk elasticity of the confined LCs. The former term scales with square of droplet size ($\propto \gamma R^2$), and the latter term scales linearly with droplet size ($\propto KR$); here γ is the interfacial tension, K is the one-constant approximated elastic constant, and R is the droplet radius.[26,32] In our experiment, $K \sim 6 \times 10^{-12}$ N[33] and $\gamma \sim 10$ mN/m, and therefore the micron-sized Janus droplets are orders of magnitude larger than the nanometer critical size, $R_0 \equiv K/\gamma$. In this regime, the interfacial energy dominates and determines the equilibrium droplet shape and cavity geometry. Therefore, in our analysis, we assume that the orientational order and elasticity of the LCs do not substantially affect "shape" at the phase boundaries. Experimentally, the excellent fits of these boundaries based on circular arcs confirm that our assumption of surface-tension dominated shape is reasonable.

3 Results and Discussion

3.1 Properties of the SmA LC Janus droplets

The SmA LC Janus droplets, which are tens of microns in diameter and dispersed in water containing surfactant SDS, were analyzed primarily by optical microscopy in this work. As detailed in the *Materials and Methods* Section 2.1, the Janus droplets were made via a phase separation scheme (Fig. 1). The SDS molecules absorbed at the 8CB-water interface impose strong homeotropic anchoring, wherein the local LC director is perpendicular to the surface. The interface between 8CB and PDMS also has homeotropic anchoring. As a result, the local SmA layers prefer to align parallel to surfaces, as indicated in inset of Fig. 1(a).

The morphologies of resultant Janus droplets are determined by the interfacial tensions $\gamma_{8\mathrm{CB-PDMS}}$, $\gamma_{8\mathrm{CB-water}}$, and $\gamma_{\mathrm{PDMS-water}}$ (*Materials and Methods* Section 2.3). By choosing the interfacial tension ratios carefully, three possible droplet morphologies can be achieved: complete engulfing (the core-shell droplet), partial engulfing (the Janus droplet), and non-engulfing (two detached droplets).[29,34] A theoretical droplet morphology state diagram is illustrated in Fig. 2(e). It presents these possibilities as a function of interfacial tension ratios, with the volume ratio between two compartments fixed to be unity. Among the controllable parameters, the ratio between interfacial tensions can be tuned by employing different compartment ingredients, or by employing a different type and amount of surfactant molecules adsorbed at the interface.

Our platform for fabricating the Janus LC droplets thus permits the control of compartment morphology and boundary conditions needed to manipulate smectic LC textures. Herein, taking note of the abundant possibilities one can potentially explore, we focus on the rich set of LC configurations that a *single* droplet morphology supports. Specifically, in this contribution, we discuss the case of droplets composed of 8CB-PDMS, with a 1:1 volume ratio, and in a 0.1 wt% SDS aqueous solution.

3.2 SmA LC textures within Janus droplets after initial quench

During initial formation of Janus drops, *i.e.*, when the hexane evaporates from the initial spherical drops containing homogeneous organic liquid mixture, a (turbulent-like) vigorous mixing was observed in the droplet as it evolved from homogeneous mixture to the targeted phase-separated Janus drop (see ESI Fig. S1† and Supplementary Video 1†). We adopt the term, "quench", to denote this entire initialization process. Note, the quench includes rapid transformation from a disordered state to an ordered LC state in the final compartment configuration. Note also, this quench is not thermal (*i.e.*, temperature is not changed), but it does have an effect that is similar to a traditional temperature quench. When the LC is dissolved in the hexane (together with PDMS) the system is isotropic, but when the solvent (hexane) is completely removed, then the LC order emerges in the form of the SmA phase.

We analyzed the SmA LC textures using bright-field optical microscopy and polarization optical microscopy (POM) (see *Materials and Methods* Section 2.2 and Fig. 2(a)), and we found them to be of three types after the quench. The LC configurations were either flower-like FCD textures (Fig. 3(b); ESI Fig. S2(a)†), dislocation ring textures (Fig. 3(c); ESI Fig. S2(b)†), or a combination of undulation and dislocation ring textures (Fig. 3(d); ESI Fig. S2(c)†). In the following subsections, we describe and characterize these texture patterns.

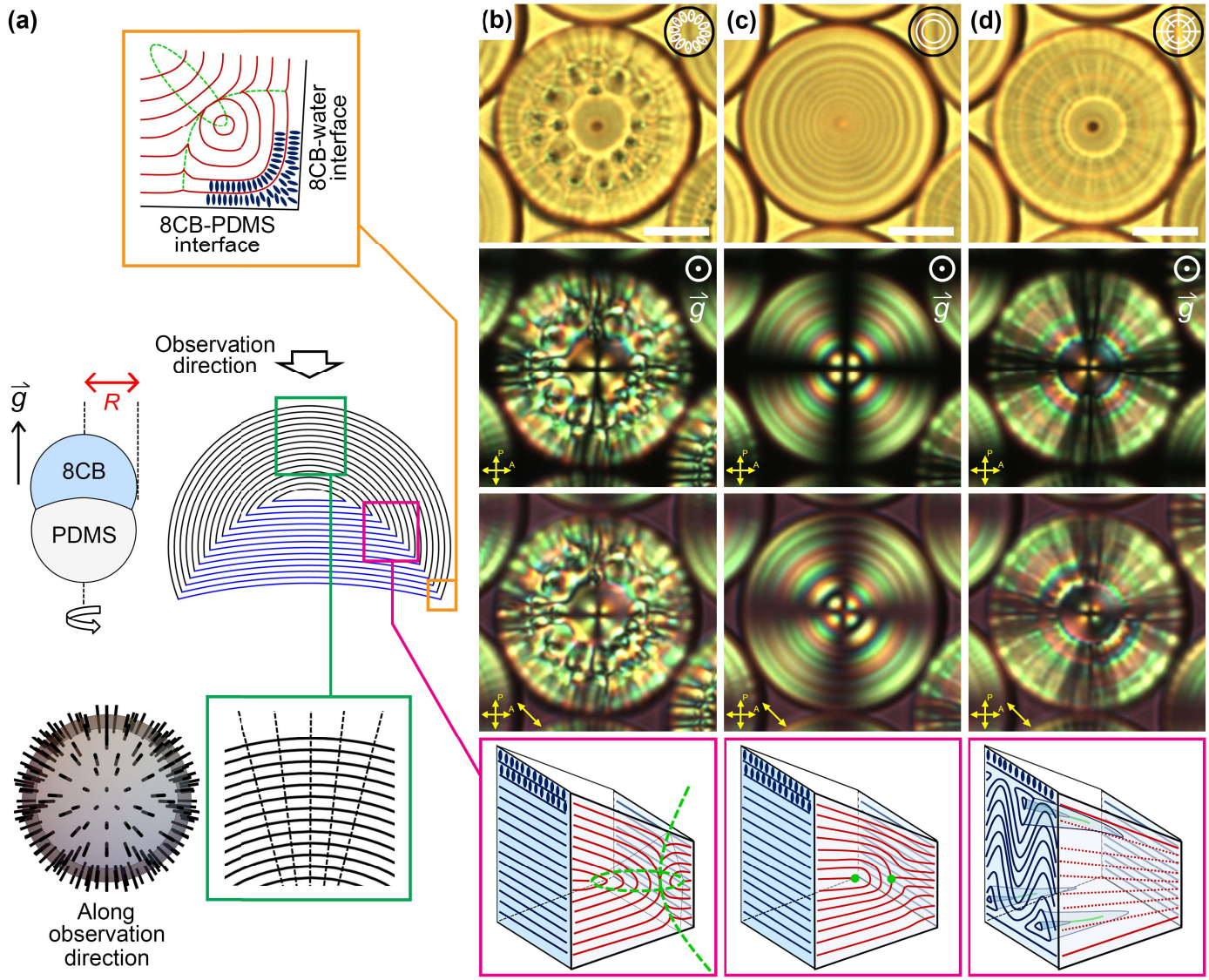

Fig. 3 SmA textures within Janus droplets. (a) Schematic in side-view of the Janus droplet (middle left) and representative smectic layers within the LC cavity (middle right). The resulting grain boundaries hint at the defect locations (magenta box). In this figure, the vector $\vec{g}$ denotes the direction of gravitational acceleration, and drop size is defined by the radius, R, of the LC compartment. Green box inset: central smectic layers arrange themselves into a family of concentric spherical domes wherein LC molecules align perpendicular to local layer surfaces (bottom panel - the solid black rods and dashed lines indicate directors in 3D). Orange box inset: at the very tip of meniscus, local SmA layers likely no longer exist (top panel). (b-d) Each column shows images of Janus droplets in bottom-view with microscope optics set for bright-field (first row), POM (second row), POM with cross-polarizers and full-wave retardation plate (third row). The images exhibit common textures for SmA LC confined in the bowl-shaped cavities of Janus droplets after the initial quench (after initial phase separation). Observed textures include (b) FCD flower-like textures, (c) dislocation ring textures, and (d) textures with both undulations and dislocation rings. Scale bar: 10 μm. Insets: schematic drawing of each texture type (bottom-view). The corresponding bottom (fourth) row schematics show how SmA layers arrange themselves to accommodate the mismatch of smectic layer numbers between drop central symmetry axis and edge (sketched as side-view, the cross sections near grain boundaries are highlighted by magenta box in (a)). In (b), the ellipse and hyperbola disclinations (green dashed curves) of the FCD are illustrated. In (c), the core region of the edge dislocation corresponds to where the defect splits into two disclinations of opposite signs (pair of green dots). In (d), only layer undulations are illustrated (*i.e.*, for simplicity, coexisting dislocation rings are not included in the schematic). Suggested segments of disclinations, extending along the drop radius, are also illustrated (green segments). Note, in POM images, black regions indicate molecular alignment parallel or perpendicular to either polarizer, and the brightest regions indicate northwest-southeast or northeast-southwest molecular alignment.

Note, the texture classification given above is based on director configurations and defect structures observed in LC compartments located far from the meniscus at the triple line, *i.e.*, far from where the 8CB-water, 8CB-PDMS, and PDMS-water interfaces meet. Though we cannot observe this region directly, at the very tip of meniscus the smectic layers likely no longer exist and, more likely, the LC molecules could reside in nematic or even isotropic phases (see Fig. 3(a) top panel; a FCD is shown in the sketch as an exemplary "last" defect near the meniscus).

Note also, despite the rich and diverse textures the system can sustain and exhibit, SmA layers around the droplet central sym-

metry axis* always arrange into a family of concentric spherical domes with 8CB molecules aligned perpendicular to local layer surfaces (Fig. 3(a) bottom panel). Observing along the symmetry axis, LC molecules tilt radially away from the axis, leading to a so-called "Maltese cross" pattern under cross-polarizers (*i.e.*, a dark cross and associated four bright lobes; see bottom-view droplet center in the second row POM images of Fig. 3(b-d)). In practice we expect the exact director configuration to vary slightly from droplet to droplet, and we expect the drop diameter and the shape of the internal 8CB-PDMS interface to vary slightly across drops. The POM image in Fig. 3(c) exhibits a dark annulus around the symmetry axis; the dark annulus suggests that the fields associated with light rays traveling through the drop (at these near-center but off-axis positions) experience a phase retardation of 2π. In the absence of significant refraction effects, this overall retardation arises from a combination of LC birefringence, LC director configuration, and the detailed Janus drop shape. These factors are expected to be at least slightly different for each drop. Additionally, the curvatures of the outer and inner interfaces are different in each drop and the off-axis light rays will generally experience different refraction (lensing) and reflection, which further complicates the retardation effects. Thus, we do not expect all drops to exhibit the same dark annulus.

3.2.1 Focal conic domain flower-like textures.

Amongst all observed SmA configurations in our setup, the FCD flower-like texture is the most visually striking (Fig. 3(b)). Previously, FCDs have been observed within planar-anchored substrates,[14–17] in free-standing droplets on surfaces,[18] in pinned liquid menisci,[19–22] in planar anchored spherical micro-emulsion drops,[25–27] and in planar anchored Janus droplets.[28] In some of these situations, FCDs also hold potential for application per topographical templates,[15,35] microlens arrays,[20,36,37] selective photomasks,[38] and superhydrophobic surfaces.[39]

In our Janus drop compartments, which have *homeotropic* anchoring, the packing that generates the observed texture is comprised of adjacent FCD "petals" arranged symmetrically around the central symmetry axis of the droplet. Within each individual FCD, SmA layers wrap around a pair of disclination (defect) curves which are conjugate conic sections: an ellipse, characterized by its eccentricity, and a hyperbola branch that passes through one focus of the ellipse. These two disclinations extend in 3D and reside in perpendicular planes; their projection into the observation focal plane gives a texture with iconic dot-within-ellipse pattern (or more specifically, short-segment-within-ellipse pattern). We observe this pattern in the bottom-view image (Fig. 3 (b); see also ESI Fig. S3†, wherein more comprehensive visualization of the individual FCD is provided).

Previously, contiguous FCD textures have been observed in spherical and Janus emulsion droplets with *parallel* anchoring conditions.[25–28] Thus, for us, it was somewhat unexpected to observe FCDs in the homeotropic-anchored Janus droplets. In our system, homeotropic anchoring arises at both the 8CB-water and 8CB-PDMS interfaces and causes the SmA layers to reconfigure parallel to the local surfaces. Since layer thickness is fixed, in the bowl-shaped geometries, more layers are required near the drop center compared to the drop edge. A spatial mismatch of layer number thus arises at various positions within the drop. Generally, the energy cost of changing the SmA layer thickness is considerably greater than that of layer bending.[25] Thus, one way for the SmA layers to ameliorate frustration due to layer number mismatch is to generate FCDs between cavity center and edge. A schematic of this texture is shown in the inset of Fig. 3(b). Notably, these FCDs in our SmA LC Janus droplets are "geometry-driven" rather than "anchoring-driven" as in prior work.[25–28]

In addition to the layer number mismatch argument, here we provide another viewpoint which offers an understanding about where the FCDs are located. Because of the homeotropic anchoring constraint, smectic layers within the bowl-shaped LC cavity can exhibit a structure similar to that of the deformed spherical onion configuration. As sketched in Fig. 3(a) middle right panel, the series of blue and black curves represent smectic layers that are parallel to and equidistant from the 8CB-PDMS and 8CB-water interfaces, respectively. A misorientation arises when these two sets of smectic layers meet but have different orientations. The resultant grain boundaries, *i.e.*, interfaces where misorientation of smectic layers occurs, can provide hints about the locations of defects (magenta box in Fig. 3(a)). The elliptic disclinations of the FCDs are likely located near these tilt grain boundaries (see ESI Fig. S4† for more details).

On the observation focal plane perpendicular to the droplet central symmetry axis, we find that FCDs pack in an uncommon manner, *i.e.*, their ellipse disclination long-axes orient radially from a common point on the central symmetry axis of droplet, by forming rings of FCDs. As suggested by Meyer *et al.*[18] and Beller *et al.*[21], such FCD flower textures (packing with non-zero eccentricity) have hyperbolae that diverge away from the structural center with no obvious intersection. Meantime, the virtual branches of the hyperbolae intersect at a common apex located on the structural symmetry axis. This observation is in contrast to the case wherein FCDs spontaneously assemble and tile space following the law of corresponding cones (LCC);[25,40–43] additionally, our observed textures cannot be explained by the traditional tilt grain boundary model[43] due to the deformed interface. In light of these factors, our observations are best explained as a construction of alternating belts of FCDs, joined smoothly onto a family of concentric spheres that share either common base or apex.[21]

Finally, for completeness we studied Janus droplets suspended in water at high SDS concentration (above CMC). In this case, the FCDs extend to the surface and exhibit bud-like internal textures (see ESI Fig. S5† and Supplementary Video 2†). Further characterization is necessary to quantify the director configurations in detail and is a subject of future work.

3.2.2 Dislocation ring texture.

The mismatch of SmA layer numbers between the Janus drop central symmetry axis and edge can accommodate simpler textures,

* The droplet central symmetry axis indicates the axis that passes through both the north (PDMS side) and south poles (8CB side) of the Janus droplet when the droplet is aligned by gravity.

i.e., simpler than the FCDs. For example, the frustration due to layer mismatch can also be relieved by introduction of edge dislocations (Fig. 3(c)). In smectics, the core region of the edge dislocation could correspond to the end of a broken layer, or it could correspond to where the defect core splits into two disclinations of opposite signs.[44,45] The separation between neighboring dislocations can be expressed as $\Lambda = b/\sin\theta = n \times d_0/\sin\theta$, where b is the Burgers vector, n is the dimensionless Burgers vector, d_0 is the smectic layer thickness, and θ is the layer misorientation angle. As a first-order approximation, we estimate $d_0 \sim 3$ nm, $\Lambda \sim 1.3$ μm, and $\theta \sim 60$ degree (obtained from Fig. 3(c) bright-field image and ESI Fig. S4(c)†, at position $r = 0.5R$ away from the droplet central symmetry axis). The dislocations reported here thus have macroscopic micron-scale Burgers vectors (*i.e.*, corresponding to a couple hundred smectic layers, which is large enough to be observed optically), suggesting that their cores would exist as two split disclinations of opposite signs.[46]

Within the bowl-shaped cavity of our Janus droplets, smectic layer number differences are readily accommodated by a series of dislocations; these dislocations extend in circular contours along the direction perpendicular to the drop radial vectors. Exemplary SmA layer configurations showing these dislocations are depicted in inset of Fig. 3(c). As long as the LC compartment/cavity retains symmetry with respect to the central drop axis, each individual dislocation will form a closed loop centered on the central symmetry axis. This property gives rise to the ring textures observed in the droplet bottom-view (Fig. 3(c)).

3.2.3 Smectic layer undulation textures.

Both the FCD flower and dislocation ring textures require energetically costly disclinations for which strain and elastic energy density grow large upon approach of the singular defect cores. It is thus important to consider whether this elastic distortion energy can be decreased, and if so, then how. Would it be possible, for example, for "defect-free" LC textures to span all or parts of the compartment cavity while still satisfying cavity geometrical and topological constraints? The answer is yes. One possible energetically cheaper solution, which appears to arise experimentally, is a third type of texture with radial undulations of the smectic layers.

Such undulating textures exhibit periodic radial striped patterns in the transmission image, as observed from the droplet bottom-view (Fig. 3(d)). The bright-dark alternation between stripes suggests that the local optical axis is rotated from its original uniform orientation, *i.e.*, the axis points in different directions in adjacent stripes. This characteristic appearance of radial wrinkles is likely due to SmA layer undulation (a buckling instability). Layer undulation commonly occurs when layers with a preferred uniform spacing are subject to dilative stress above a certain threshold.[47,48] In such cases, the free energy of the smectic LC is minimized by generation of undulating layers. In the present case, this stress arises from the bowl-shaped geometry, a scenario similar to that previously proposed for systems with various shapes.[49–52]

By contrast to the FCD flower and dislocation ring textures, which are accommodated by topological defects, when the layer number in a given slice (cross-section) of the bowl-shaped cavity is constant, then the geometrical constraint is equivalent to a dilation, and dilation can cause the LC director to bend. This dilative stress will be more severe closer to the drop center. Since director bending is prohibited in the SmA phase, once above a critical stress, the SmA layers will undulate to fill space and relax stress. As schematically indicated in inset of Fig. 3(d), the smectic layers buckle progressively and increasingly along radial direction toward droplet central symmetry axis (*i.e.*, along the direction of maximum cavity thickness change). Our observations also suggest that segments of disclinations extending along droplet radius could potentially arise to fill the troughs between adjacent buckles. As a result, to best accommodate the bowl-shaped geometry, the corresponding "effective" thickness at drop center could be greater than simply the sum of individual smectic layers.

Note, the pure undulation scenario described above is best suited to cavities with small thickness gradients. In practice, the SmA layer undulation texture can combine with the dislocation ring texture to fulfill the geometrical requirements of the Janus droplets. Our observations suggest that this type of combination texture does indeed arise in practice and might be the lowest free energy texture for this system.

3.3 Metastable SmA textures

Thus far, we have described, classified, and explained three types of SmA LC textures that form after the first quench to create the Janus LC drops. Here we report on measurements of the occurrence and character of the SmA textures as a function of droplet size, defined by the radius, R, of the 8CB compartment (illustrated in left panel sketch of Fig. 3). As indicated in Fig. 4(a), the very largest drops only sustain FCD textures; similarly, the very smallest drops only sustain dislocation ring textures. For an intermediate range of drop sizes ($R \approx 7.5{\sim}17.5$ μm), all three textures are found.

The occurrence frequency of the different textures under different conditions raises questions about SmA texture stability and free energy. Here we are most interested in ranking the free energy of these different textures. To elucidate this issue, we employed a microfluidics setup to fabricate Janus droplets with monodisperse size $R = 15.4$ μm, thereby enabling systematic analysis of the population of each texture. The left column of the bar chart in Fig. 4(b) exhibits the percentage of occurrence of FCD flower textures, dislocation ring textures, and undulation textures (which typically coexist with dislocation ring textures) from a pool of ~100 droplets. The observations show that after quenching, for the intermediate-size drops, more than 50% have a radial undulation texture; among the rest, the dislocation ring texture is a little more likely than the FCD texture. Moreover, all configurations are stable over time in the absence of perturbations. These clues suggest that several *metastable* SmA textures can form, and that those with undulations (which typically coexist with dislocation ring textures) might have the lowest free energy.

We also explored the possibility that different cavity geome-

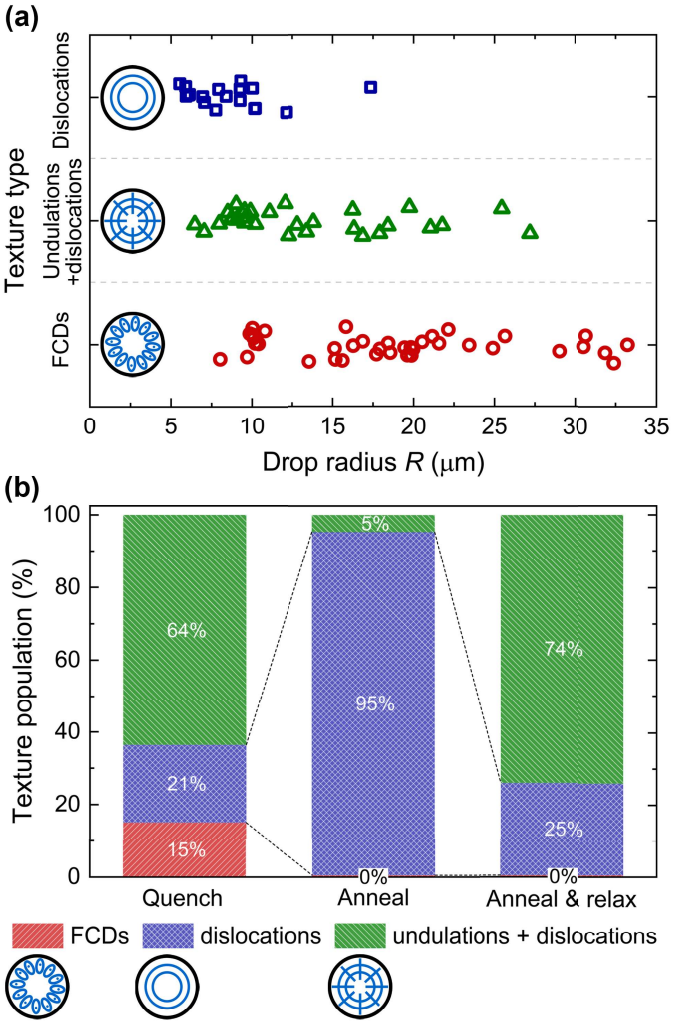

Fig. 4 Occurrence of different SmA textures with respect to drop size and their evolution after quenching, after annealing, and after annealing/relaxation. (a) Occurrence of FCD flower textures (bottom row, red circles), textures of undulations plus dislocation rings (middle row, green triangles), and dislocation ring textures (top row, blue squares) as a function of Janus droplet size. These samples were made by the simple shaking method, and the observations were made after the first quench. Each data point represents one measurement from a droplet. Note, vertical axis jittering of the data has been added to each texture type to permit better visualization of closely packed data points. (b) The population (percent occurrence) of each texture type measured after the first quench (left column), after annealing (middle column), and after annealing and further relaxation (right column). Within each individual column, the occurrence percentage of FCD flower textures, dislocation ring textures, and textures of undulations plus dislocation rings are represented by red, blue, and green color, respectively. These data were gathered from a pool of ~100 droplets with monodisperse radius $R = 15.4\ \mu$m, fabricated by microfluidics.

tries could be associated with particular metastable SmA textures. Specifically, we fit the phase boundaries of Janus droplet cavities, and from these fits we calculated interfacial tension ratios (see *Materials and Methods* Section 2.3). These studies suggest that somewhat different cavity morphologies arise for droplets that contain different textures (Fig. 5(a)). Distinguishing between droplets that contain dislocation rings or undulations plus dislocation rings is difficult, but droplets with FCDs were relatively easy to distinguish from the other two cases.

The plot of $\gamma_{8CB-PDMS}/\gamma_{PDMS-water} - \gamma_{8CB-water}/\gamma_{PDMS-water}$ suggests that the occurrence of FCD textures is accompanied by larger interfacial tension at both 8CB-water and 8CB-PDMS boundaries, but especially at the 8CB-water interface. This larger interfacial tension could be caused by the FCD textures themselves, or it could arise during drop formation (the quench and rapid mixing process) wherein a cavity geometry that slightly favors formation of FCD textures is created. We speculate that the observed increase in interfacial tension could be caused by the deviation of LC directors near the surface from their preferred homeotropic anchoring, which, in turn, would diminish the oc-

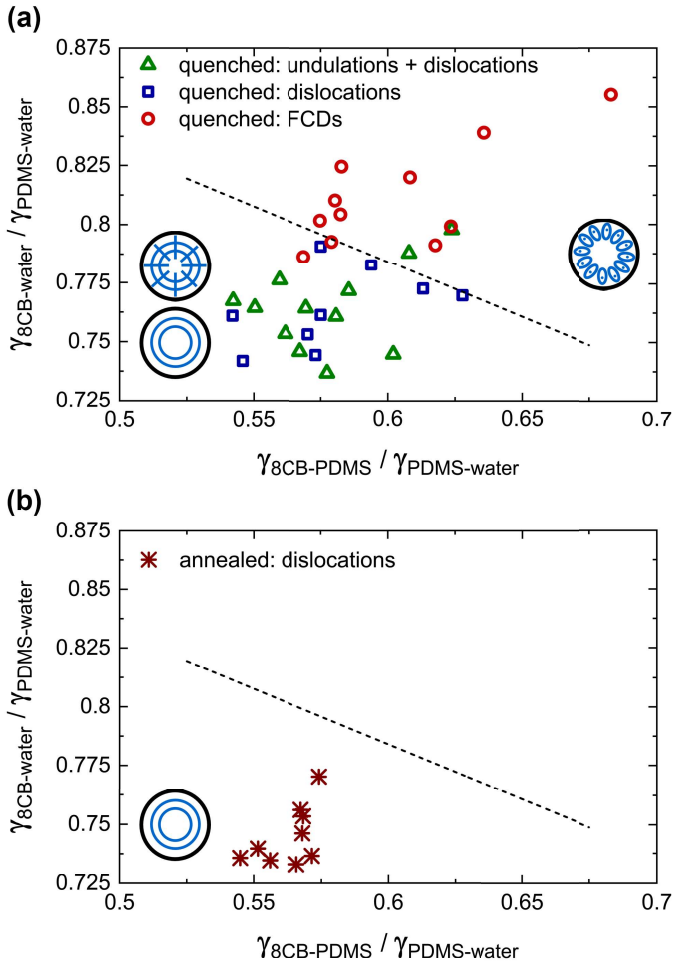

Fig. 5 Cavity morphologies and interfacial tensions for Janus drops containing different SmA textures after the first quench and after annealing. (a) Plot of $\gamma_{8CB-PDMS}/\gamma_{PDMS-water} - \gamma_{8CB-water}/\gamma_{PDMS-water}$ for the Janus drops after the initial quench (and concurrent phase separation). The experimentally determined ratios between interfacial tensions are connected to the observed textures within individual Janus drop cavity. The green triangles, blue squares, and red circles indicate drops containing textures of undulations plus dislocation rings, dislocation ring textures, and FCD flower textures, respectively. The black dashed line roughly separates regimes of FCD drops and dislocation/undulation drops and is drawn to guide the eye. (b) Plot of $\gamma_{8CB-PDMS}/\gamma_{PDMS-water} - \gamma_{8CB-water}/\gamma_{PDMS-water}$ for Janus drops after annealing. For this case, only drops containing dislocation ring textures were observed (represented by dark red stars). The same black dashed line as shown in (a) is given for comparison.

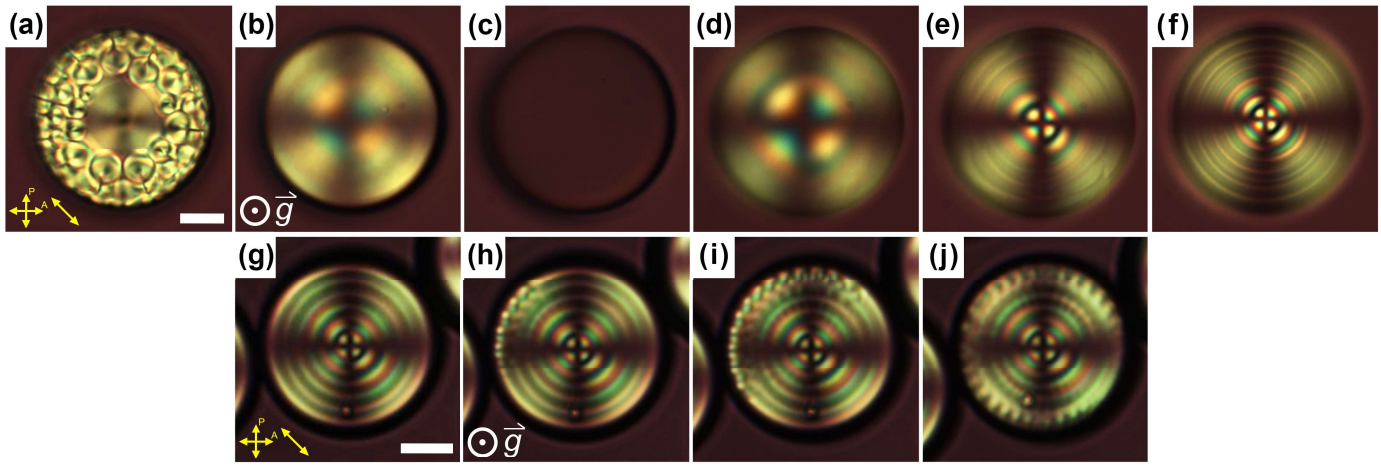

Fig. 6 SmA texture evolution/transition during thermal annealing and relaxation. (a-c) FCD flower textures (achieved after the initial quench) melt as the system temperature is increased so that the 8CB undergoes a phase transition from SmA phase through nematic phase to the isotropic phase. (d) The temperature is then decreased slowly again and the LCs "pre-align" with a radial configuration in the nematic phase. (e-f) Further cooling then leads to formation of dislocation ring textures in the SmA phase. Note, the FCD textures do not reoccur after annealing. (g-j) Occasionally, smectic undulations could be observed to appear on top of the existing dislocation rings and further "relax" the SmA droplets into their final equilibrium states. All POM images were recorded between cross-polarizers with a full-wave retardation plate. Note, the image snapshots in (a-f) and (g-j) were bottom-view and taken from two different droplets. Also, the focal plane varies slightly between images, which leads to an apparent slightly different drop size. Scale bar: 10 μm.

currence of well-aligned interfacial molecular packings.[53–56] In principle, the FCDs could induce more substantial interfacial distortions than either the dislocations or the layer undulations; the greater distortion is then associated with a less ordered interface, which leads to larger interfacial tension. Further characterization by experiment or theory/simulation is necessary to confirm these speculations about microscopic mechanisms.

3.4 Metastable SmA textures evolve after annealing and relaxation

As noted in the previous section, the three observed SmA textures after the first quench appear to suggest the existence of several metastable textures. To address the question of metastability, we employed a thermal annealing process. In essence, the thermal annealing process heats 8CB into its isotropic phase, and then the sample is cooled slowly so that 8CB condenses sequentially into its nematic phase and finally its SmA phase. Such heating-cooling schemes provide an opportunity for the LC molecules to rearrange and achieve their (potentially) lowest free energy configuration in the cavity.

Interestingly, by far the most common texture of the annealed drops was the dislocation ring texture (see middle column in Fig. 4(b)). FCD textures were never observed after annealing. We thus suggest that the FCD textures are metastable and could be the most energetically costly texture of the three. An exemplary droplet displaying the texture transition from FCD flower textures (forming upon quench) to dislocation ring textures (after annealing) is shown in Fig. 6(a-f) and ESI Supplementary Video 3†.

Although the data are not unambiguous, we propose that formation of metastable FCDs upon quench is due to the (turbulent-like) vigorous mixing within the droplet that occurs during phase separation (discussed in Section 3.2; also consult ESI Fig. S1† and Supplementary Video 1†). Vigorous hydrodynamic flows randomize the system transiently during the quench, and the relatively short time interval for formation of ordered states likely prevents the SmA LC from reaching its equilibrium configuration. In addition, once formed, the high viscosity of 8CB causes texture reformation kinetics to be extremely slow. That is, the rapid increase of viscosity following fast Janus droplet formation slows relaxation of molecular rearrangement (as has been observed elsewhere in different lamellar phases[57]). The annealing procedure, by contrast, melts the LC compartment into the disordered isotropic phase and then cools slowly enough to permit the system to remain close to equilibrium. Importantly, the "pre-alignment" of LC directors in the nematic phase, *i.e.*, at early stage of the cooling process, helps lock the LC molecules into their final alignment in the bulk. Note, in the nematic phase, the LCs exhibit a radial configuration with a point defect at drop cavity center. As the temperature decreases further, the SmA layers then rearrange based on an already partially ordered structure. We confirmed the more consistent and narrowly distributed morphology of these annealed Janus droplets by fitting their phase boundaries, which agree well with the quenched droplets containing dislocation rings (dark red stars in Fig. 5(b)).

Finally, when these annealed Janus droplets, which mostly contain dislocation rings, are further "relaxed" at room temperature for another few days without interruption, we found that a large portion of the droplets undergo another texture transformation into the combination state of undulations plus dislocation rings (see right column in Fig. 4(b)). Evidently, the transition arises because the existing SmA structures and dislocation disclinations cannot fully satisfy the geometric and anchoring boundary conditions. As a result, further modulation in the smectic phase is desirable to lower the free energy. Since extra smectic layers or disclinations cost energy, and because layer undulation offers a fast way for the system to relax in the presence of stress,[52,58,59]

the layer undulations gradually increase from droplet edge toward center (see radial striped patterns characterized in Section 3.2.3) until the boundary conditions are completely fulfilled (see Fig. 6(g-j) and ESI Supplementary Video 4†).

4 Conclusions

We fabricated SmA LC Janus droplets with homeotropic anchoring, consisting of two immiscible compartments: the smectic LC 8CB and PDMS. The SmA LC in the cavities relaxed to specific stable/metastable textures, and we experimentally analyzed the resulting textures, their frequency of occurrence, and their spatiotemporal evolution under various (processing) conditions. We observed three categories of SmA textures: FCD flowers, dislocation rings, and undulations plus dislocation rings. All observed textures, either with or without topological defects, arise to fulfill interfacial boundary conditions of the cavity, especially the geometric constraints. Frustration relief was driven primarily by the need to accommodate layer number mismatch between drop center and edge. Notably, previous methods to generate FCDs in suspended droplets have exploited interfacial *planar anchoring*. The present method, by contrast, is based on compartmental "geometry-driven" effects in *homeotropic-anchored* emulsion droplets.

Our observations suggest that cavity geometry, boundary conditions, and drop fabrication procedures can lead to occurrence of *metastable* smectic textures. During formation of Janus drops, the fast and vigorous phase-separation process prevents the smectic from reaching its equilibrium state. Thermal annealing, by contrast, enables the system to evolve towards lower free energy states. Amongst these configurations (and for drops with radius in the intermediate 15∼35 micron-diameter range), FCD flowers are likely the most energetically costly texture and are associated with larger 8CB-water interfacial tension. The texture with dislocation rings plus smectic layer undulations appears to be the energetically cheapest morphology and is associated with smaller 8CB-water interfacial tension. Note, this proposed energy ranking derives primary support from experimental observations. However, in principle the differences in the occurrence frequency of different texture types before and after annealing could arise from the associated state energy, from kinetic pathway, or a combination thereof. Theoretical modeling is required before we can unambiguously confirm the energy ground states of the system.

Although the equilibrium ground state has not been unambiguously determined, our investigation found that the different LC texture types could be created, controlled, and even converted from one texture to another via different fabrication pathways. To our knowledge, most previous studies suggest that LCs confined in emulsion droplets quickly settle into a single equilibrium configuration. Our findings are unusual in this respect and offer new routes for crafting soft matter structures. For example, smectics with artificially-made defect ordering [15,20,35–39] have been recently suggested as a new class of soft building blocks, but consideration of the effects of kinetics are absent from the current approach. In general, relatively little is known about how various defect textures could arise from different fabrication pathways and be converted from one texture to another. The possibility to precisely control LC defect/texture formation and subsequent *evolution* expands our tool-kit for fabricating functional soft materials. More broadly, different kinetic routes could lead to different intermediated states, which might even help us optimize the chemical reactions and synthesis processes carried out in the confined spaces of microreactors.

Looking to the future, the study of texture formation dynamics teaches us more about how smectic layers accommodate confinement frustration. Our preliminary observations suggested that the smectic textures always form and fill the entire available cavity in a sequential manner (see Fig. 6(e-f) & (g-j) and ESI Supplementary Video 3† & Video 4†). More work is needed to gain quantitative understanding for prediction of energetics of observed metastable textures and detailed packing rules for FCDs. Moreover, it would be interesting to explore how these smectic textures configure and reconfigure due to either external fields or tunable anchoring conditions. The existing system could also serve as a template for embedded nanoparticles for photonic applications. [60]

Author Contributions

W.-S.W., J.J., P.J.C. and A.G.Y. conceived the idea and designed the experiments. W.-S.W. and J.J. initiated and performed the experiments. W.-S.W., J.J., P.J.C. and A.G.Y. worked on different facets of the data analysis. W.-S.W. and A.G.Y. wrote the paper, and all authors contributed to the final manuscript.

Conflicts of Interest

The authors declare no competing interests.

Acknowledgements

We thank Kevin B. Aptowicz, Zoey S. Davidson, Alexis de la Cotte, Remi Dreyfus, Sophie Ettinger, Piotr Habdas, Yi-Yun Ho, Randall D. Kamien, Daeyeon Lee, Angel Martinez, and Francesca Serra for helpful discussions. We acknowledge financial support from the National Science Foundation (grant no. DMR20-03659), the Materials Research Science & Engineering Center (MRSEC) at University of Pennsylvania (grant no. DMR17-20530) including MRSEC's Optical Microscopy Shared Experimental Facility, and NASA (grant no. 80NSSC19K0348). J.J. acknowledge financial support from the National Research Foundation of Korea (grant no. NRF-2021R1A2C1011163).

References

1 M. V. Kurik and O. D. Lavrentovich, *Sov. Phys. Usp.*, 1988, **31**, 196-224.

2 O. D. Lavrentovich, Y. A. Nastishin, V. I. Kulishov, Y. S. Narkevich, A. S. Tolochko and S. V. Shiyanovskii, *Europhys. Lett.*, 1990, **13**, 313-318.

3 I. Dierking, *Textures of Liquid Crystals*, John Wiley & Sons, Weinheim, 2003.

4 G. Toquer, T. Phou, S. Monge, A. Grimaldi, M. Nobili and C. Blanc, *J. Phys. Chem. B*, 2008, **112**, 4157-4160.

5 K. Peddireddy, P. Kumar, S. Thutupalli, S. Herminghaus and C. Bahr, *Langmuir*, 2013, **29**, 15682-15688.

6 P. J. Collings and J. W. Goodby, *Introduction to Liquid Crystals: Chemistry and Physics*, 2nd. Ed., Crc Press, New York, 2019.

7 W.-S. Wei, Y. Xia, S. Ettinger, S. Yang and A. G. Yodh, *Nature*, 2019, **576**, 433-436.

8 K. Peddireddy, S. Čopar, K. V. Le, I. Muševič, C. Bahr and V. S. R. Jampani, *Proc. Natl. Acad. Sci. USA*, 2021, **118**.

9 T. Lopez-Leon and A. Fernandez-Nieves, *Colloid Polym. Sci.*, 2011, **289**, 345-359.

10 S. H. Ryu and D. K. Yoon, *Liquid Crystals*, 2016, **43**, 1951-1972.

11 M. Urbanski, C. G. Reyes, J. Noh, A. Sharma, Y. Geng, V. S. R. Jampani and J. P. F. Lagerwall, *J. Phys.: Condens. Matter*, 2017, **29**, 133003.

12 J. B. Fournier and G. Durand, *J. Phys. II France*, 1991, **1**, 845-870.

13 R. Pratibha and N. V. Madhusudana, *J. Phys. II France*, 1992, **2**, 383-400.

14 M. C. Choi, T. Pfohl, Z. Wen, Y. Li, M. W. Kim, J. N. Israelachvili and C. R. Safinya, *Proc. Natl. Acad. Sci. USA*, 2004, **101**, 17340-17344.

15 D. K. Yoon, M. C. Choi, Y. H. Kim, M. W. Kim, O. D. Lavrentovich and H. T. Jung, *Nat. Mater.*, 2007, **6**, 866-870.

16 Y. H. Kim, D. K. Yoon, M. C. Choi, H. S. Jeong, M. W. Kim, O. D. Lavrentovich and H. T. Jung, *Langmuir*, 2009, **25**, 1685-1691.

17 A. Honglawan, D. A. Beller, M. Cavallaro, R. D. Kamien, K. J. Stebe and S. Yang, *Adv. Mater.*, 2011, **23**, 5519-5523.

18 C. Meyer, L. Le Cunff, M. Belloul and G. Foyart, *Materials*, 2009, **2**, 499-513.

19 M. A. Gharbi, I. B. Liu, Y. Luo, F. Serra, N. D. Bade, H. N. Kim, Y. Xia, R. D. Kamien, S. Yang and K. J. Stebe, *Langmuir*, 2015, **31**, 11135-11142.

20 F. Serra, M. A. Gharbi, Y. Luo, I. B. Liu, N. D. Bade, R. D. Kamien, S. Yang and K. J. Stebe, *Adv. Optical Mater.*, 2015, **3**, 1287-1292.

21 D. A. Beller, M. A. Gharbi, A. Honglawan, K. J. Stebe, S. Yang and R. D. Kamien, *Phys. Rev. X*, 2013, **3**, 041026.

22 M. A. Gharbi, D. A. Beller, N. Sharifi-Mood, R. Gupta, R. D. Kamien, S. Yang and K. J. Stebe, *Langmuir*, 2018, **34**, 2006-2013.

23 J. Jeong and M. W. Kim, *Phys. Rev. Lett.*, 2012, **108**, 207802.

24 J. Jeong and M. W. Kim, *Appl. Phys. Lett.*, 2012, **101**, 061914.

25 O. D. Lavrentovich, *Sov. Phys. JETP*, 1986, **64**, 1666-1676.

26 C. Blanc and M. Kleman, *Eur. Phys. J. E*, 2001, **4**, 241-251.

27 G. Lee, F. Araoka, K. Ishikawa, Y. Momoi, O. Haba, K. Yonetake and H. Takezoe, *Part. Part. Syst. Charact.*, 2013, **30**, 847-852.

28 A. Concellón, C. A. Zentner and T. M. Swager, *J. Am. Chem. Soc.*, 2019, **141**, 18246-18255.

29 J. Jeong, A. Gross, W.-S. Wei, F. Tu, D. Lee, P. J. Collings and A. G. Yodh, *Soft Matter*, 2015, **11**, 6747-6754.

30 P. B. Umbanhowar, V. Prasad and D. A. Weitz, *Langmuir*, 2000, **16**, 347-351.

31 J. Jeong, E. Um, J. K. Park and M. W. Kim, *RSC Adv.*, 2013, **3**, 11801-11806.

32 I. Muševič, *Liquid Crystal Colloids*, Springer, New York, 2017.

33 M. J. Bradshaw, E. P. Raynes, J. D. Bunning and T. E. Faber, *J. Phys. France*, 1985, **46**, 1513-1520.

34 J. Guzowski, P. M. Korczyk, S. Jakiela and P. Garstecki, *Soft Matter*, 2012, **8**, 7269-7278.

35 Y. H. Kim, D. K. Yoon, H. S. Jeong and H. T. Jung, *Soft Matter*, 2010, **6**, 1426-1431.

36 Y. H. Kim, H. S. Jeong, J. H. Kim, E. K. Yoon, D. K. Yoon and H. T. Jung, *J. Mater. Chem.*, 2010, **20**, 6557-6561.

37 J. H. Kim, Y. H. Kim, H. S. Jeong, M. Srinivasarao, S. D. Hudson and H. T. Jung, *RSC Adv.*, 2012, **2**, 6729-6732.

38 Y. H. Kim, J. O. Lee, H. S. Jeong, J. H. Kim, E. K. Yoon, D. K. Yoon, J. B. Yoon and H. T. Jung, *Adv. Mater.*, 2010, **22**, 2416-2420.

39 Y. H. Kim, D. K. Yoon, H. S. Jeong, J. H. Kim, E. K. Yoon and H. T. Jung, *Adv. Funct. Mater.*, 2009, **19**, 3008-3013.

40 G. Friedel, *Ann. Phys. Paris*, 1922, **9**, 273-474.

41 W. Bragg, *Nature*, 1934, **133**, 445-456.

42 J. P. Sethna and M. Kléman, *Phys. Rev. A*, 1982, **26**, 3037.

43 M. Kléman and O. D. Lavrentovich, *Eur. Phys. J. E*, 2000, **2**, 47-57.

44 C. E. Williams and M. Kléman, *J. Phys. Colloq.*, 1975, **36**, C1-315.

45 H. Aharoni, T. Machon and R. D. Kamien, *Phys. Rev. Lett.*, 2017, **118**, 257801.

46 M. Kléman and O. D. Laverntovich, *Soft Matter Physics: An Introduction*, Springer Science & Business Media, New York, 2007.

47 N. A. Clark and R. B. Meyer, *Appl. Phys. Lett.*, 1973, **22**, 493-494.

48 M. Delaye, R. Ribotta and G. Durand, *Phys. Lett. A*, 1973, **44**, 139-140.

49 M. Conradi, P. Ziherl, A. Šarlah and I. Muševič, *Eur. Phys. J. E*, 2006, **20**, 231-236.

50 H. L. Liang, S. Schymura, P. Rudquist and J. Lagerwall, *Phys. Rev. Lett.*, 2011, **106**, 247801.

51 T. Lopez-Leon, A. Fernandez-Nieves, M. Nobili and C. Blanc, *Phys. Rev. Lett.*, 2011, **106**, 247802.

52 M. Selmi, J. C. Loudet, P. V. Dolganov, T. Othman and P. Cluzeau, *Soft Matter*, 2017, **13**, 3649-3663.

53 H. Kasten and G. Strobl, *J. Chem. Phys.*, 1995, **103**, 6768-6774.

54 M. Tintaru, R. Moldovan, T. Beica and S. Frunza, *Liquid Crystals*, 2001, **28**, 793-797.

55 X. Li and M. M. Denn, *Macromolecules*, 2002, **35**, 6446-6454.

56 P. K. Rai, M. M. Denn and C. Maldarelli, *Langmuir*, 2003, **19**, 7370-7373.

57 R. Guégan, D. Morineau, R. Lefort, W. Béziel, M. Guendouz, L. Noirez, A. Henschel and P. Huber, *Eur. Phys. J. E*, 2008, **26**, 261-273

58 P. G. de Gennes and J. Prost, *The Physics of Liquid Crystals*, 2nd. Ed., Clarendon Press, Oxford, 1993.

59 P. Oswald and P. Pieranski. *Smectic and Columnar Liquid Crystals: Concepts and Physical Properties Illustrated by Experiments*, Taylor & Francis, Boca Raton, 2005.

60 L. Tran, H. N. Kim, N. Li, S. Yang, K. J. Stebe, R. D. Kamien and M. F. Haase, *Sci. Adv.*, 2018, **4**, eaat8597.